
Article:
Forrester, J. orcid.org/0000-0002-8102-7576, Davidson, J. and Foster, M.P. (2023) Inductorless step-up piezoelectric resonator (SUPR) converter: a describing function analysis. IEEE Transactions on Power Electronics, 38 (10). pp. 12874-12885. ISSN 0885-8993

https://doi.org/10.1109/TPEL.2023.3294802

Inductorless Step-up Piezoelectric Resonator (SUPR) Converter: a Describing Function Analysis

Jack Forrester, Jonathan N. Davidson and Martin P. Foster

Abstract—A model for an inductorless step-up piezoelectric-resonator-based DC-DC (SUPR) converter is presented. A describing function approach is used to determine the equivalent circuit of the MOSFET power stage and resonator, allowing the duty cycles of both MOSFETs to be accurately estimated. The model provides a method for estimating the output voltage and resonant current of the converter during operation. The accuracy of the model is verified against experimental and simulation results, with a less than 1.5% mean absolute percentage error in voltage gain estimation, compared to experimental measurements. Design guidelines for optimal operation of the converter are also presented.

Index Terms—DC-DC converters, Design Optimization, Piezoelectric Devices, Resonant Converters, Zero Voltage Switching (ZVS).

I. Introduction

Piezoelectric-based resonant converters are an alternative to traditional resonant converters, offering several advantages including high power density, high efficiency, low EMI content and the ability to be used in harsh environments [1]–[4]. Piezoelectric devices make use of the direct and converse piezoelectric effects, allowing the transformation of energy from mechanical to electrical and vice versa, respectively. The use of piezoelectric devices in power converters has seen an increase in interest in the past few decades, with improvements to piezoelectric materials leading to performance comparable with traditional magnetic transformer based converters [5].

The most popular piezoelectric device used in resonant power conversion is the piezoelectric transformer (PT). A PT has an input and an output section, with electrodes attached to these sections, which are each formed from one or more layers of piezoelectric material, depending on the PT topology. PTs exhibit high Q factors, have inherent resonant circuits and transformers, making them ideal for use in resonant converters. Several applications of piezoelectric transformers (PTs) have been presented such as cold-cathode fluorescent lamp drivers, battery chargers and circuitry for liquid crystal displays [1], [6]–[8]. PTs suffer from the need for multiple layers, which significantly complicates their manufacture.

Typically, magnetic resonant converters use frequency and duty cycle to control the output voltage (PFM, PWM control) [9]. However, voltage regulation is challenging for high Q converters because the ZVS ability is highly sensitive to changes in duty cycle and frequency. In [8], to ensure ZVS with a piezoelectric transformer-based converter, a fixed phase difference between resonant current and switching signals, and a switching arrangement involving 25% on time and 25% off time with two 25% duration deadtime intervals between is used. Control methods [10]–[12] have been developed for PT based converters but are complex to implement and can lead to performance degradation.

This work was supported by the Engineering and Physical Sciences Research Council under grant EP/S031421/1.

The authors are with the Department of Electronic and Electrical Engineering, University of Sheffield, Sheffield, UK (e-mail: Jack.Forrester@sheffield.ac.uk, Jonathan.Davidson@sheffield.ac.uk, M.P.Foster@sheffield.ac.uk).

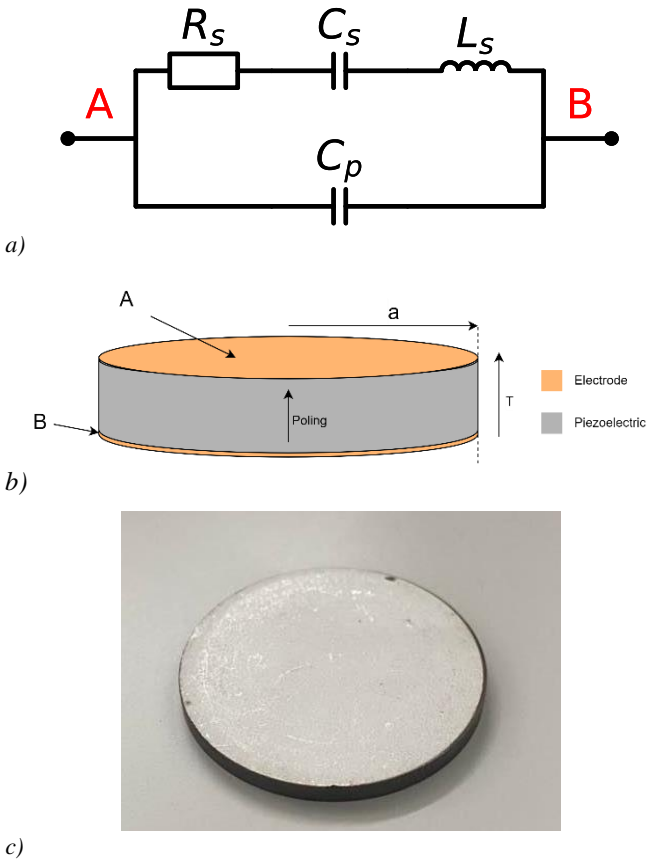

Fig. 1 – a) Piezoelectric resonator equivalent circuit, b) Radial mode PR schematic, c) SMD30T21F1000S Piezo resonator

Piezoelectric resonator-based converters provide an alternative way of utilising piezoelectric devices in resonant converters, whilst avoiding some of the complexities involved in PT based converters. Piezoelectric resonators (PRs) can be formed from a single layer of ceramic and, as such, they are equivalent to the input section of a PT. PRs also have high quality (Q) factors, often higher than PTs owing to their simpler construction Whilst exhibiting some advantages over PTs, Piezoelectric resonator (PR) devices only possess two

terminals, meaning they do not have an integrated transformer for voltage transformation and as a result they do not provide galvanic isolation. Additionally, similar to PTs, they suffer from additional spurious resonant modes, which can interfere with the operation of a PR based converter [13].

In most PR based converters, the PR acts as a resonating energy store much like the inductor in a boost converter: it accumulates and releases energy according to the instantaneous circuit conditions [14]. The equivalent circuit of the piezoelectric resonator is shown in Fig. 1a. Nodes A and B represent the electrodes of the device, C_p is the electrode capacitance, C_s and L_s represent the mechanical resonance and R_s models the damping.

Current work on PRs has been focused around developing new converter topologies. Pollet et al [14] presented a novel piezoresonator based boost converter, showing significant voltage gain and good efficiency. Boles et al [15] presented several new topologies of PR converters, each offering unique operating voltage ranges, efficiencies and output voltages. Touhami et al [16] presented a new PR converter offering improved performance over those presented by Boles et al, with an output power of 175W at 80% efficiency, significantly higher output power than previous PR converters and higher than PT based converters [17]. These proposed converters do not require magnetic inductors to operate efficiently and can operate over a wider range of voltage conversion ratios than the inductorless half-bridge PT converter.

Other work by Boles et al and Touhami et al focuses on optimal material choice for high power and high efficiency PRs [18], [19]. Authors have subsequently presented control schemes for the proposed PR converters, Piel et al [20] presented a simple feedback controller for a step-down converter topology presented in [14], based on either sensing the PR voltage or by using fixed time durations for each of the switching modes. Both Touhami et al [21] and Forrester et al [22] present control strategies for the PR based converters presented in [16] and [14], respectively. Both papers use comparators and voltage sensing to determine optimal timings for each of the MOSFETs within the converter. In [21] the authors focus on regulating the output voltage using a PI controller, whereas in [22] the authors focused on optimising the operating frequency using a phase-locked loop (PLL).

The converter described in [14] and [23] is named here as the inductorless step-up piezoelectric resonator (SUPR) converter for convenience. It is of particular interest as it can be used for step-up power conversion of DC supplies. Unlike the PT-based half-bridge resonant converter, the SUPR can achieve ZVS under a wide variety of operating conditions if a suitable controller is used.

Modelling of resonant converters is often performed to assist the design process of the converter. Many methods of analysing PT-based resonant converters have been presented in the literature. These method include a parametric analysis [24], which allow the ZVS characteristics of a PT converter to be estimated. However, this method requires a number of assumptions to be made, limiting its application. Cyclic mode analysis [25] is also commonly used and provides accurate estimation of voltages and current in a PT based converter. One downside to cyclic mode modelling is that only numerical solutions can be found. Parametric sweeps and curve fitting [26] have also be employed, where PT parameters are varied and the resulting converter simulated (using SPICE), the results are then curve fit against the varied parameters to estimate a simplified equation for the ZVS characteristics, offering an approximate analytical solution. However, this method can get overly complex when assessing many variables and by not considering all variables can make the resulting equation inaccurate. A describing function approach using fundamental mode analysis [27] was also used to analyse the inductorless half-bridge PT based converter offering a good balance of accuracy and complexity to achieve a very simplified equation for designing PTs for achieving ZVS. As a result, the modelling in this paper will use a similar describing function approach.

In [15], Boles et al applied a modelling approach to several topologies of PR converter. However, obtaining an accurate estimation of the switch timings using this method requires the solution of 15 equations with 18 variables, which is highly computationally complex. In [14], Pollet et al present a model for the SUPR converter, deriving expressions for the voltage gain and piezoelectric current amplitude, which contain only a small number of variables (circuit parameters and control variables). However, whilst offering a simple expression, operating frequency is an input variable and not calculated by the model. Owing to the high Q factor, operating frequency has a significant effect on the operation of PR converters, therefore, additional steps should be taken to determine the optimal operating frequency when using this model. Additionally, both models do not include the effects of semiconductor losses, leading to inaccuracy.

In this paper a derivation and evaluation of an analytical model of the SUPR converter is presented using a describing function approach. The operation of the SUPR converter is discussed and decomposed into six distinct operating modes. A piecewise description of the resonator input voltage, v_{C_p}, is derived in terms of circuit component values and mode durations. The optimal mode durations for given operating conditions (load and output voltage) are estimated by analysing energy conservation, charge conservation and using a describing function approximation of the resonator voltage. Unlike previous approaches, this analysis then allows the optimum switch conduction times and optimum operating frequency to be found for any set of circuit parameters. In addition, solving for mode durations only requires solving a single equation with only 4 unknowns, a large reduction compared to previous approaches. The model is compared to experimental and Simulink results for particular component values. From this analysis, guidelines for design and control are provided.

II. Operation of Converter

Fig. 2 shows the circuit diagram for the piezoelectric-resonator boost converter with the resonator being represented by the equivalent circuit within the dashed box. The operating waveforms for the converter are shown in Fig. 3, with the start of a cycle ($\theta = 0$) being the positive zero crossing of resonant current i_{L_s} (*note that this current is equivalent to the particle velocity in the piezoelectric resonator; it cannot be measured directly*). A cycle is divided into six modes of operation

depending on the conduction states of the diodes and the control of the MOSFET switches. The circuit is driven at an operating frequency f such that the zero crossings of the resonant current i_{L_s} occur at $\theta = 0,\ \theta_3 = \pi, \theta_6 = 2\pi$ with a period $T = 1/f = 2\pi/\omega$.

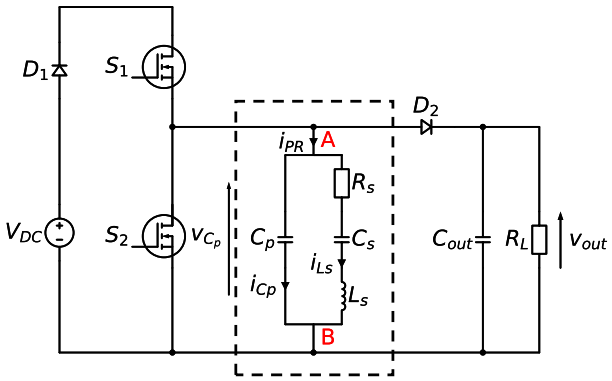

Fig. 2 – Piezoelectric-resonator-based boost converter

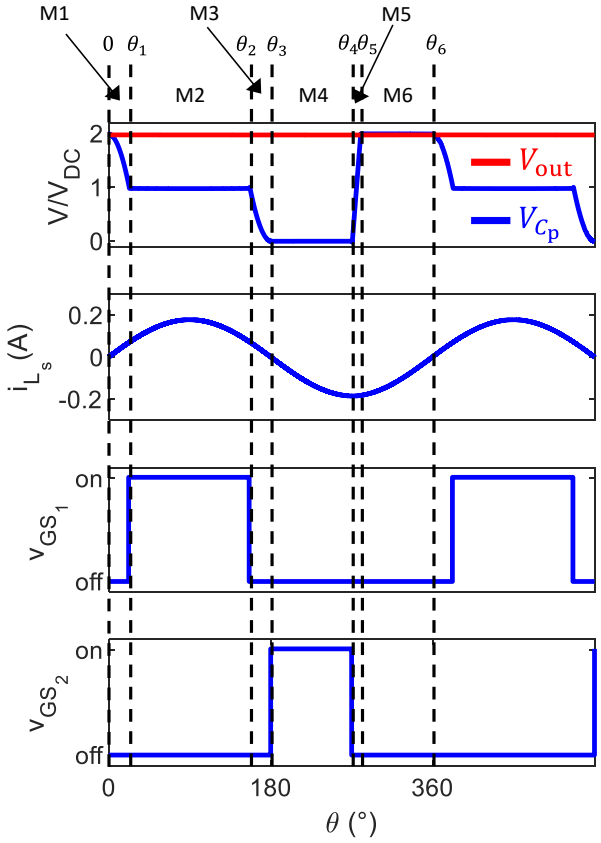

Fig. 3 – Typical operating waveforms for the piezoelectric resonator-based boost converter

The six modes of operation M1 → M6 for this converter during ideal operation are:—

M1 ($0 \rightarrow \theta_1$): Prior to start of a cycle, D_2 is conducting such that $v_{C_p}(0) = V_{\text{out}} + V_{\text{df}}$, where V_{out} is the output voltage and V_{df} is the forward voltage drops of D_1 and D_2. Both MOSFETs S_1 and S_2 are turned off at $\theta = 0$, as the current i_{L_s} undergoes a positive zero crossing. During M1, i_{L_s} circulates within the PR discharging C_p and causing v_{C_p} to decrease until it reaches $V_{\text{DC}} - V_{\text{df}}$. Since $v_{C_p} < V_{\text{out}}$, D_2 is naturally turned off at $\theta = 0$ and so C_{out} provides the energy to the load.

M2 ($\theta_1 \rightarrow \theta_2$): At θ_1, $v_{C_p} = V_{\text{DC}} - V_{\text{df}}$ and so S_1 is turned on under ZVS condition. Energy is supplied to the resonator through S_1 during M2.

M3 ($\theta_2 \rightarrow \theta_3$): S_1 is turned off at θ_2. θ_3 is chosen to allow sufficient time for i_{L_s} to discharge v_{C_p} to 0.

M4 ($\theta_3 \rightarrow \theta_4$): At θ_3, i_{L_s} undergoes a negative zero crossing and, if the conditions are correct, $v_{C_p}(\theta_3) = 0$. Therefore, S_2 turns-on at θ_3 under ZVS condition. During M4, $v_{C_p} \approx 0$ and i_{L_s} flows through S_2.

M5 ($\theta_4 \rightarrow \theta_5$): At θ_4, S_2 is turned off, the negative i_{L_s} charges C_p thereby increasing v_{C_p}. At θ_5, $v_{C_p} = V_{\text{out}} + V_{\text{df}}$.

M6 ($\theta_5 \rightarrow \theta_6$): $v_{C_p} = V_{\text{out}} + V_{\text{df}}$, D_2 is forward-biased, thus energy is provided from the resonator to R_L and C_{out}. At $\theta_6 = 2\pi$, i_{L_s} undergoes another positive zero crossing and the cycle repeats.

III. MODEL DERIVATION

In this section a model is derived for the SUPR converter, allowing the output voltage, resonant current and resonator voltage (v_{C_p}) to be estimated. The derivation begins by developing a piecewise equation for v_{C_p} based on the resonant current, mode angles and equivalent circuit component values. During operation, θ_4 (or the S_2-conduction angle, $(\theta_4 - \pi)$) is used to control the voltage gain of the converter. We will therefore assume θ_4 is fixed by some external controller and is an input to the model. The unknown mode angles (θ_1, θ_2 and θ_5) are found, allowing the converter operation to be modelled across a cycle and allowing metrics such as output voltage and resonant current to be determined.

The unknown mode angles are determined by solving simultaneous equations (named J_1, J_2, J_3 and J_4) which are derived based on diode commutation conditions, energy balance, output charge conservation and by equating the signal-based fundamental mode impedance of the resonator to the circuit-based impedance using a describing-function approximation of the v_{C_p}. Thus, the resulting four simultaneous equations can be solved numerically to find the three unknown mode angles and operating frequency. Finally, equations are derived for the output voltage and resonant current amplitude based on the mode angles and equivalent circuit component values thereby completing the model to allow V_{out}, v_{C_p} and i_{L_s} to be estimated for any PR based converter.

A. *Developing a piecewise model for v_{C_p}*

In the derivation that follows it is assumed that the PR is constructed using high quality factor piezoelectric material ($Q \gg 1$) thus the PR is considered to be a highly selective band-pass filter. Under these assumptions, the PR current i_{L_s} is sinusoidal and is defined as

$$i_{L_s} = I_{L_s} \sin(\theta) \tag{1}$$

where I_{L_s} is the amplitude of the resonant current, i_{L_s}. During modes M1, M3 and M5, the power devices are off and so i_{L_s}

circulates through C_p charging or discharging it. It should be noted that the MOSFET drain-source capacitance also appears in parallel with C_p. v_{C_p} during these modes is given by

$$v_{C_\mathrm{p}}(\theta) = \frac{1}{\omega C_\mathrm{p}} \int -i_{L_\mathrm{s}}\,\mathrm{d}\theta = \frac{I_{L_s}\cos(\theta)}{\omega C_\mathrm{p}} + V_i \tag{2}$$

where i is the mode number, V_i is the constant of integration associated with the mode and ω is the operating frequency (rad s^{-1}). We assume that the resonant current crosses through zero at $0, \theta_3$ and θ_6 and $C_\mathrm{p} \gg C_\mathrm{DS}$, where C_DS is the MOSFET drain-source capacitance.

In M1, V_1 can be found by solving (2) with $v_{C_\mathrm{p}}(0) = V_\mathrm{out} + V_\mathrm{df}$, thus giving

$$V_1 = V_\mathrm{out} + V_\mathrm{df} - \frac{I_{L_s}}{\omega C_\mathrm{p}} \tag{3}$$

where we assume the output voltage V_out is constant. Thus, for M1,

$$v_{C_\mathrm{p}} = \frac{I_{L_s}(\cos\theta - 1)}{\omega C_\mathrm{p}} + V_\mathrm{out} + V_\mathrm{df} \qquad 0 \le \theta < \theta_1 \tag{4}$$

In M2, S_1 is on, allowing energy to be injected into the resonator through S_1 and D_1 and, thus, v_{C_p} is clamped to the supply voltage, less the diode forward voltage drop and the voltage drop across the R_{DS_on} of the switch,

$$v_{C_\mathrm{p}} = V_\mathrm{DC} - V_\mathrm{df} - I_{L_\mathrm{s}} R_{DS_\mathrm{on}} \sin\theta \qquad \theta_1 \le \theta < \theta_2 \tag{5}$$

In M3, S_1 is off and i_{L_s} circulates through C_p discharging it to 0 at $\theta_3 = \pi$. V_3 can be found by considering $v_{C_\mathrm{p}}(\theta_2) = V_\mathrm{DC} - V_\mathrm{df} - I_{L_\mathrm{s}} \sin\theta_2\, R_{DS_\mathrm{on}}$

$$V_3 = V_\mathrm{DC} - V_\mathrm{df} - I_{L_\mathrm{s}}\left(R_{DS_\mathrm{on}} \sin\theta_2 + \frac{\cos(\theta_2)}{\omega C_\mathrm{p}}\right) \tag{6}$$

Thus,

$$v_{C_\mathrm{p}} = V_\mathrm{DC} - V_\mathrm{df} + I_{L_\mathrm{s}}\left(\frac{\cos\theta - \cos\theta_2}{\omega C_\mathrm{p}} - R_{DS_\mathrm{on}} \sin\theta_2\right) \qquad \theta_2 \le \theta < \pi \tag{7}$$

In M4, S_2 is on and the v_{C_p} voltage is clamped at 0, minus the voltage drop across the R_{DS_on} of the switch, therefore

$$v_{C_\mathrm{p}} = -I_{L_\mathrm{s}} R_{DS_\mathrm{on}} \sin\theta \qquad \pi \le \theta < \theta_4 \tag{8}$$

In M5, S_2 has turned off and i_{L_s} charges C_p. V_5 can be found solving $v_{C_\mathrm{p}}(\theta_4) = -I_{L_\mathrm{s}} \sin\theta_4\, R_{DS_\mathrm{on}}$

$$V_5 = -I_{L_s}\left(\frac{\cos\theta_4}{\omega C_\mathrm{p}} + R_{DS_\mathrm{on}} \sin\theta_4\right) \tag{9}$$

Thus

$$v_{C_\mathrm{p}} = I_{L_\mathrm{s}}\left(\frac{\cos\theta - \cos\theta_4}{\omega C_\mathrm{p}} - R_{DS_\mathrm{on}} \sin\theta_4\right) \qquad \theta_4 \le \theta < \theta_5 \tag{10}$$

Finally, during M6, v_{C_p} is given by

$$v_{C_\mathrm{p}} = V_\mathrm{out} + V_\mathrm{df} \qquad \theta_5 \le \theta < 2\pi \tag{11}$$

A piecewise description of the v_{C_p} voltage can be written

$$v_{C_\mathrm{p}} = \begin{cases} V_\mathrm{out} + V_\mathrm{df} + \frac{I_{L_\mathrm{s}}}{\omega C_\mathrm{p}}(\cos\theta - 1) & 0 \le \theta < \theta_1 \\ V_\mathrm{DC} - V_\mathrm{df} - I_{L_\mathrm{s}} R_{DS_\mathrm{on}} \sin\theta & \theta_1 \le \theta < \theta_2 \\ I_{L_\mathrm{s}}\left(\frac{\cos\theta - \cos\theta_2}{\omega C_\mathrm{p}} - R_{DS_\mathrm{on}} \sin\theta_2\right) + V_\mathrm{DC} - V_\mathrm{df} & \theta_2 \le \theta < \pi \\ -I_{L_\mathrm{s}} R_{DS_\mathrm{on}} \sin\theta & \pi \le \theta < \theta_4 \\ I_{L_\mathrm{s}}\left(\frac{\cos\theta - \cos\theta_4}{\omega C_\mathrm{p}} - R_{DS_\mathrm{on}} \sin\theta_4\right) & \theta_4 \le \theta < \theta_5 \\ V_\mathrm{out} + V_\mathrm{df} & \theta_5 \le \theta < 2\pi \end{cases} \tag{12}$$

B. Finding mode angles

In order to generate the v_{C_p} waveform and calculate the output voltage and resonant current amplitude, the unknown mode angles (θ_1, θ_2 and θ_5) and the operating frequency (ω) need to be determined.

1) Output capacitance charge conservation

In steady state there is no change in the output capacitor voltage from the end of one cycle to the end of the next (i.e. $V_\mathrm{out}(t) = V_\mathrm{out}(t+T)$). Thus, the charge transferred through D_2, denoted by Q_{D_2}, must balance with the charge that is delivered to the load, Q_load over a whole cycle. Charge is transferred through D_2 only during M6. The current i_{D_2} during conduction is given by,

$$i_{\mathrm{D}_2} = i_{D_1} - i_{L_\mathrm{s}} - i_{C_\mathrm{p}} \tag{13}$$

During M6, S_1 is off, therefore $i_{\mathrm{D}_1} = 0$. Similarly, since v_{C_p} is constant $\frac{\mathrm{d}v_{C_\mathrm{p}}}{\mathrm{d}t} = 0 \Rightarrow i_{C_\mathrm{p}} = 0$. Therefore, $i_{\mathrm{D}_2} = -i_{L_\mathrm{s}}$ during M6. Thus, an equation for the charge through D_2 is given by,

$$Q_{\mathrm{D}_2} = \frac{1}{\omega}\int_{\theta_5}^{2\pi} -i_{L_\mathrm{s}}\mathrm{d}\theta = \frac{I_{L_\mathrm{s}}(1 - \cos\theta_5)}{\omega} \tag{14}$$

Since I_out is consumed by the load, the charge delivered to the load over the course of one cycle is given by

$$Q_\mathrm{load} = I_\mathrm{out} T = 2\pi \frac{I_\mathrm{out}}{\omega} = 2\pi \frac{V_\mathrm{out}}{R_L \omega} \tag{15}$$

Therefore, equating Q_{D_2} (14) and Q_{load} (15) and rearranging gives an equation for V_{out},

$$V_{\mathrm{out}} = \frac{I_{L_\mathrm{s}} R_L (1 - \cos\theta_5)}{2\pi} \tag{16}$$

Another equation for V_{out} can be generated by noting that $v_{C_\mathrm{p}}(\theta_5) = V_{\mathrm{out}} + V_{\mathrm{df}}$, thus, by substituting $v_{C_p}(\theta_5) = V_{\mathrm{out}} + V_{\mathrm{df}}$ into (10) and rearranging,

$$V_{\mathrm{out}} = -V_{\mathrm{df}} + I_{L_\mathrm{s}} \left(\frac{\cos\theta_5 - \cos\theta_4}{\omega C_\mathrm{p}} - R_{\mathrm{DS_{on}}} \sin\theta_4 \right) \tag{17}$$

Both (16) and (17) are dependent on I_{L_s}. An expression for I_{L_s} can be found by substituting $v_{C_\mathrm{p}}(\pi) = 0$ into (7),

$$V_{\mathrm{DC}} = V_{\mathrm{df}} + I_{L_\mathrm{s}} \left(\frac{\cos\theta_2 + 1}{\omega C_\mathrm{p}} + R_{\mathrm{DS_{on}}} \sin\theta_2 \right) \tag{18}$$

Then, (18) can be rearranged for I_{L_s} giving,

$$I_{L_\mathrm{s}} = \frac{V_{DC} - V_{\mathrm{df}}}{\frac{\cos\theta_2 + 1}{\omega C_\mathrm{p}} + R_{\mathrm{DS_{on}}} \sin\theta_2} \tag{19}$$

Finally, by subtracting (16) from (17), and using (19) gives the first simultaneous equation J_1 in terms of circuit components and mode angles

$$J_1 = 0 \tag{20}$$

where

$$\begin{aligned} J_1 = &-\left(\omega C_\mathrm{p} R_\mathrm{L} + 2\pi\right)\cos\theta_5 + 2\pi\cos\theta_4 \\ &+ 2\pi\omega C_\mathrm{p} R_{\mathrm{DS_{on}}} \sin\theta_4 \\ &+ \frac{1}{V_{\mathrm{dc}} - V_{\mathrm{df}}} \left(2\pi V_{\mathrm{df}} \left[\cos\theta_2 \right.\right. \\ &\left.\left. + \omega C_\mathrm{p} R_{\mathrm{DS_{on}}} \sin\theta_2 + \left\{ 1 - \frac{R_\mathrm{L}\omega C_\mathrm{p}}{2\pi} \right\} \right] \right. \\ &\left. + \omega C_\mathrm{p} R_\mathrm{L} V_{\mathrm{dc}} \right) \end{aligned} \tag{21}$$

2) Energy conservation

The second simultaneous equation J_2 is developed based on energy conservation. The energy into the converter will equal the energy supplied to the load plus the losses in the circuit.

Energy is supplied to the resonator during M2, therefore an equation for the input energy is given by

$$E_{\mathrm{in}} = \frac{1}{\omega} \int_{\theta_1}^{\theta_2} i_{L_\mathrm{s}}(\theta) V_{DC} \, d\theta \tag{22}$$

Evaluating this gives,

$$E_{\mathrm{in}} = \frac{I_{L_\mathrm{s}} V_{DC} (\cos(\theta_1) - \cos(\theta_2))}{\omega} \tag{23}$$

Similarly, an equation for the energy delivered to the load can be derived by noting that energy is transferred to the load throughout the whole cycle, thus

$$E_{\mathrm{out}} = \frac{1}{\omega} \int_0^{2\pi} \frac{V_{\mathrm{out}}^2}{R_\mathrm{L}} \mathrm{d}\theta = \frac{2\pi V_{\mathrm{out}}^2}{\omega R_\mathrm{L}} \tag{24}$$

An equation for the energy dissipated in the resonator is given by

$$E_{\mathrm{R_{s_{Loss}}}} = \frac{R_\mathrm{S}}{\omega} \int_0^{2\pi} I_{L_\mathrm{s}}^2 \sin^2(\theta) \, \mathrm{d}\theta = \frac{I_{L_\mathrm{s}}^2 R_\mathrm{S} \pi}{\omega} \tag{25}$$

Additionally, we also consider the conduction losses in the two MOSFETs (we assume ZVS thus no switching losses). Conduction losses occur when the MOSFET is conducting, thus equations for these losses are given by

$$\begin{aligned} E_{\mathrm{S_{1_{Loss}}}} &= \frac{R_{\mathrm{DS_{on}}}}{\omega} \int_{\theta_1}^{\theta_2} I_{L_\mathrm{s}}^2 \sin^2(\theta) \, \mathrm{d}\theta \\ &= \frac{I_{L_\mathrm{s}}^2 R_{\mathrm{DS_{on}}}}{2\omega} \left(\theta_2 - \theta_1 \right. \\ &\left. + \frac{1}{2}(\sin 2\theta_2 - \sin 2\theta_1) \right) \end{aligned} \tag{26}$$

$$\begin{aligned} E_{\mathrm{S_{2_{Loss}}}} &= \frac{R_{DS_{\mathrm{on}}}}{\omega} \int_{\pi}^{\theta_4} \left[I_{L_\mathrm{s}} \sin(\theta) \right]^2 \mathrm{d}\theta \\ &= \frac{I_{L_\mathrm{s}}^2 R_{DS_{\mathrm{on}}}}{2\omega} \left(\theta_4 - \pi - \frac{\sin 2\theta_4}{2} \right) \end{aligned} \tag{27}$$

Finally, we also consider the conduction losses in the two diodes. Conduction losses occur when the diode is conducting thus equations for these losses are given by

$$\begin{aligned} E_{D_{1\mathrm{Loss}}} &= \frac{V_{\mathrm{df}}}{\omega} \int_{\theta_1}^{\theta_2} I_{L_\mathrm{s}} \sin(\theta) \, \mathrm{d}\theta \\ &= \frac{V_{\mathrm{df}} I_{L_\mathrm{s}} (\cos\theta_1 - \cos\theta_2)}{\omega} \end{aligned} \tag{28}$$

$$E_{D_{2\mathrm{Loss}}} = \frac{V_{\mathrm{df}}}{\omega} \int_{\theta_5}^{2\pi} I_{L_\mathrm{s}} \sin(\theta) \, \mathrm{d}\theta = \frac{V_{\mathrm{df}} I_{L_\mathrm{s}} (\cos\theta_5 - 1)}{\omega} \tag{29}$$

where V_{df} is the diode forward voltage drop. Therefore, due to energy conservation, the input energy is equated to the output energy plus losses

$$\begin{aligned} E_{\mathrm{in}} = E_{\mathrm{out}} + E_{\mathrm{R_{s_{Loss}}}} + E_{\mathrm{S_{1_{Loss}}}} + E_{\mathrm{S_{2_{Loss}}}} + E_{D_{1\mathrm{Loss}}} \\ + E_{D_{2\mathrm{Loss}}} \end{aligned} \tag{30}$$

Substituting (16), (23)-(29) into (30) gives (35). (19) is used to eliminate I_{L_s} in (35), then by rearranging to move all terms on to the right-hand side, gives the second simultaneous equation J_2

$$J_2 = 0 \tag{31}$$

Where J_2 is defined in (36).

3) Describing function for v_{C_p}

A third equation for the mode angles can be generated by equating the signal-based equivalent impedance of the resonant circuit to the component-based impedance of the resonant circuit. The signal-based impedance is generated by first performing fundamental mode analysis to generate a describing function approximation of the v_{C_p} voltage, $v_{C_\mathrm{p}<1>}$.

We define the fundamental component (FC) of a waveform as its first term of the Fourier series which in general can be written as

$$v_x(\theta) \overset{\mathrm{FC}}{\rightarrow} V_{x<1>} = \frac{1}{\pi}\int_0^{2\pi} v_x(\theta) e^{-\mathrm{j}\theta}\,\mathrm{d}\theta \tag{32}$$

$v_{C_\mathrm{p}<1>}$ is evaluated using the piecewise description of v_{C_p} given in (12) and the result simplified using (16) and (18). The resulting equation for $v_{C_\mathrm{p}<1>}$ has been omitted due to length and instead is written as a function of its dependent variables

$$v_{C_\mathrm{p}<1>} = f\left(I_{L_\mathrm{s}}, V_\mathrm{df}, C_\mathrm{p}, R_\mathrm{L}, \omega, \theta_1, \theta_2, \theta_4, \theta_5\right) \tag{33}$$

A Python script for generating $v_{C_\mathrm{p}<1>}$ using the SymPy library [28] is provided in the Appendix. The signal-based impedance can then be calculated using (19) and Ohm's law, with the result given in (34).

$$Z_{SB} = \frac{v_{C\mathrm{p}<1>}}{I_{L_\mathrm{s}}} = g\left(V_\mathrm{df}, C_\mathrm{p}, R_\mathrm{L}, \omega, \theta_1, \theta_2, \theta_4, \theta_5\right) \tag{34}$$

We assume this impedance provides a good model of the converter under its particular operating conditions. The component-based impedance of the piezoelectric resonator is given by

$$Z_{CB} = \mathrm{j}\omega L_\mathrm{s} + \frac{1}{\mathrm{j}\omega C_\mathrm{s}} + R_\mathrm{s} \tag{37}$$

Since Z_{SB} and Z_{CB} will be equal under our assumption (and close in practice), $0 = Z_{SB} - Z_{CB}$. Substituting (37), into this gives

$$0 = Z_{SB} - \mathrm{j}\omega L_\mathrm{s} - \frac{1}{\mathrm{j}\omega C_\mathrm{s}} - R_\mathrm{s} \tag{38}$$

An equation for J_3 is generated by subtracting the imaginary part from the real part of (38), which must both equal 0.

$$J_3 = 0 \tag{39}$$

$$\begin{aligned} J_3 = \Re\left(Z_{SB} - \mathrm{j}\omega L_\mathrm{s} - \frac{1}{\mathrm{j}\omega C_\mathrm{s}} - R_\mathrm{s}\right) \\ - \Im\left(Z_{SB} - \mathrm{j}\omega L_\mathrm{s} - \frac{1}{\mathrm{j}\omega C_\mathrm{s}} - R_\mathrm{s}\right) \end{aligned} \tag{40}$$

4) Turn-on angle of S_1

As the v_{C_p} waveform is continuous, then at the end of M1 $v_{C_\mathrm{p}}(\theta_1^-) = v_{C_\mathrm{p}}(\theta_1^+)$. Substituting (12) into this and rearranging for V_DC gives

$$V_\mathrm{DC} = 2V_\mathrm{df} + V_\mathrm{out} + I_{L_\mathrm{s}}\left(\frac{\cos\theta_1 - 1}{\omega C_\mathrm{p}} + R_{\mathrm{DS_{on}}}\sin\theta_1\right) \tag{41}$$

V_out is eliminated by substituting (16) into (41)

$$\begin{aligned} V_\mathrm{DC} = 2V_\mathrm{df} + I_{L_\mathrm{s}}\left(\frac{\cos\theta_1 - 1}{\omega C_\mathrm{p}} + R_{\mathrm{DS_{on}}}\sin\theta_1\right. \\ \left. - \frac{R_L(\cos\theta_5 - 1)}{2\pi}\right) \end{aligned} \tag{42}$$

Finally, substituting (18) into (42) and using (19) to eliminate I_{L_s}, the result is rearranged to move all terms on to the right-hand side, giving an equation for the fourth and final simultaneous equation J_4

$$\begin{aligned} &2\pi\left(I_{L_s} + \omega C_\mathrm{p} I_{L_s} R_{\mathrm{DS_{on}}}\sin\theta_2 + \omega C_\mathrm{p} V_\mathrm{df} + I_{L_s}\cos\theta_2\right)\frac{\cos\theta_1 - \cos\theta_2}{\omega C_\mathrm{p}} \\ &\quad = I_{L_s} R_L \cos^2\theta_5 + \left(2\pi V_\mathrm{df} - 2I_{L_s}R_L\right)\cos\theta_5 + \pi\left(2V_\mathrm{df} + I_{L_s}R_{\mathrm{DS_{on}}}\sin\theta_1\right)\cos\theta_1 \\ &\quad - \pi\left(2V_\mathrm{df} + I_{L_s}\sin\theta_2\, R_{\mathrm{DS_{on}}}\right)\cos\theta_2 - \pi I_{L_s} R_{\mathrm{DS_{on}}}\cos\theta_4\sin\theta_4 + 2\pi^2\left(R_s - \frac{R_{\mathrm{DS_{on}}}}{2}\right)I_{L_s} \\ &\quad - \pi\left(2V_\mathrm{df} - R_{\mathrm{DS_{on}}}(\theta_2 + \theta_4 - \theta_1)I_{L_s}\right) + I_{L_s}R_L \end{aligned} \tag{35}$$

$$\begin{aligned} J_2 = \frac{1}{V_\mathrm{DC} - V_\mathrm{df}}\Big(&-\omega C_\mathrm{p}(V_\mathrm{DC} - V_\mathrm{df})R_L\cos^2\theta_5 - 2\pi(V_\mathrm{DC} - V_\mathrm{df})\cos^2\theta_2 \\ &- \left((-2V_\mathrm{DC} + 2V_\mathrm{df})\cos\theta_1 + 2V_\mathrm{df}\cos\theta_5 + \omega C_\mathrm{p}(V_\mathrm{DC} - V_\mathrm{df})R_{\mathrm{DS_{on}}}\sin\theta_2 + 2V_\mathrm{DC} - 4V_\mathrm{df}\right)\pi\cos(\theta_2) \\ &- \pi(V_\mathrm{DC} - V_\mathrm{df})\left(\omega C_\mathrm{p} R_{\mathrm{DS_{on}}}\sin\theta_1 - 2\omega C_\mathrm{p} R_{\mathrm{DS}_{on}}\sin\theta_2 - 2\right)\cos\theta_1 \\ &+ \left(-2\pi\omega C_\mathrm{p} V_\mathrm{df} R_{\mathrm{DS_{on}}}\sin\theta_2 - 2\pi V_\mathrm{df} + 2\omega C_\mathrm{p}(V_\mathrm{DC} - V_\mathrm{df})R_L\right)\cos\theta_5 + 2\pi\omega C_\mathrm{p} V_\mathrm{df} R_{\mathrm{DS_{on}}}\sin\theta_2 \\ &+ \pi\omega C_\mathrm{p}(V_\mathrm{DC} - V_\mathrm{df})R_{\mathrm{DS_{on}}}\cos\theta_4\sin\theta_4 - 2\pi^2\omega C_\mathrm{p}(V_\mathrm{DC} - V_\mathrm{df})\left(R_s - \frac{R_{\mathrm{DS_{on}}}}{2}\right) \\ &+ \pi\left(-\omega C_p R_{\mathrm{DS_{on}}}(V_\mathrm{DC} - V_\mathrm{df})(\theta_2 + \theta_4 - \theta_1) + 2V_\mathrm{df}\right) - \omega C_\mathrm{p}(V_\mathrm{DC} - V_\mathrm{df})R_L\Big) \end{aligned} \tag{36}$$

$$J_4 = 0 \tag{43}$$

where J_4 is defined as,

$$\begin{aligned} J_4 = \frac{1}{V_{DC} - V_{\mathrm{df}}}\big(&2\pi(V_{\mathrm{DC}} - 2V_{\mathrm{df}})\big(\cos\theta_2 \\ &+ \omega C_{\mathrm{p}} R_{DS_{\mathrm{on}}} \sin\theta_2\big) + 4\pi V_{DC} \\ &- 6\pi V_{\mathrm{df}}\big) \\ &+ \omega C_{\mathrm{p}}\big(R_{\mathrm{L}}\cos\theta_5 - 2\pi R_{DS_{\mathrm{on}}}\sin\theta_1\big) \\ &- 2\pi\cos\theta_1 - C_{\mathrm{p}} R_{\mathrm{L}}\omega \end{aligned} \tag{44}$$

5) Calculating mode angles

A non-linear minimisation is performed on a cost function comprising of equations (21), (36), (40) and (44) as below,

$$J_{\mathrm{sum}} = J_1^2 + J_2^2 + J_3^2 + J_4^2 \tag{45}$$

where $J_{\mathrm{sum}} = 0$ is achieved with ideal mode angles and at the ideal operating frequency. Since model precision and component tolerances provide limits to any model, the minimum value of J_{sum} is the closest approximation. The sequential quadratic programming (SQP) algorithm is used within MATLAB (the *FMINCON* function) to find the unknowns, including optimal mode angles (θ_1, θ_2, θ_5) and operating frequency (ω). The SQP algorithm is a state of the art non-linear solving method, outperforming other algorithms in terms of efficiency and accuracy [29]. A series of logical constraints are used: $0 \le \theta_1 \le \theta_2 \le \pi$, $\theta_4 \le \theta_5 \le 2\pi$ and $\omega \ge 1/\sqrt{L_{\mathrm{s}}C_{\mathrm{s}}}$. Initial estimates are used as follows: $\omega = 1/\sqrt{L_{\mathrm{s}}C_{\mathrm{s}}}$, $\theta_1 = \pi/10$. $\theta_2 = 3\pi/10$, $\theta_5 = \theta_4 + \pi/20$ where θ_4 is an input to the cost function. Although this process is involved, it is still significantly less computationally intensive than previously presented methods.

C. Finding I_{L_s}, V_{out} and V_{C_p}

Based on the calculated mode angles and operating frequency, the output voltage and resonant current amplitude can be found, after which the $v_{C_{\mathrm{p}}}$ waveform can be plotted. To find V_{out}, (19) is substituted in to (17) and simplified giving

$$\begin{aligned} V_{\mathrm{out}} = \frac{1}{\sin\theta_2\, R_{\mathrm{DS_{on}}}\omega C_{\mathrm{p}} + \cos(\theta_2) + 1}\big((&V_{\mathrm{DC}} \\ &- V_{\mathrm{df}}\big)\big(\cos\theta_4 - \cos\theta_5 \\ &+ \omega C_{\mathrm{p}} R_{\mathrm{DS_{on}}}\sin\theta_4\big) \\ &- V_{\mathrm{df}}\big(1 + \omega C_{\mathrm{p}}\sin\theta_2\, R_{\mathrm{DS_{on}}} \\ &+ \cos\theta_2\big)\big) \end{aligned} \tag{46}$$

Finally, (19) and (46) can be substituted into (12) leaving an expression for $v_{C_{\mathrm{p}}}$ exclusively in terms of circuit component values, mode angles and frequency, thus allowing the whole $v_{C_{\mathrm{p}}}$ waveform to be evaluated.

IV. Experimental Verification

To verify the proposed model, a practical piezo resonator-based converter is constructed using the Steminc SMD30T21F1000S piezo resonator shown in Fig. 1b. The equivalent circuit properties of this resonator, given in Table 1, were extracted from impedance measurements taken using an Omicron Bode 100 vector network analyser, using the characterisation technique described in [30].

A SUPR converter was constructed using IRF510 MOSFETs (with an IR2110 gate drive IC), 1N5819 diodes, a 12V DC supply is used and $C_{\mathrm{out}} = 10\mu\mathrm{F}$. The converter is driven by a PLL-based controller which synchronises the MOSFET switching events to the resonant current $i_{L_{\mathrm{s}}}$. Since $i_{L_{\mathrm{s}}}$is internal to the PR, a current estimator is required, as presented in [22]. The current estimator measures the current through the PR ($i_{L_{\mathrm{s}}} + i_{C_{\mathrm{p}}}$) and subtracts the estimated current through C_p ($i_{C_{\mathrm{p}}}$), giving an estimate of the resonant current ($i_{L_{\mathrm{s}}}$). The zero crossings of the estimated resonant current are extracted using a comparator to give a square wave, which is in-phase with the resonant current.

A Xilinx PYNQ FPGA is used to control the converter. This FPGA contains both programmable logic (PL) and a microprocessor (PS) running Linux. The PS runs a web server allowing communication with both the PS and PL using a python script. First, a simple all digital PLL is implemented on the FPGA, which subsequently locks onto the estimated resonant current of the PR, producing a square wave to drive the rest of the logic.

S_2 is comparatively easy to drive, the MOSFET turns on at the falling edge of the PLL output signal and operates with a fixed duty cycle, which is controlled by a python script. Two comparators are used to generate a signal when the PR voltage drops is $\le V_{\mathrm{DC}}$ and ≤ 0. S_1 turns on when the PR voltage equals V_{DC}, then the duty cycle of S_1 is adjusted by a control loop on the FPGA, to cause the PR voltage to cross equal 0 just before S_2 turns on. Additional elements are also included to account for propagation delays, noisy signals and to stop shoot-through. Full details of the operation of the controller is described in [22].

Table 1 - SMD30T21F1000S equivalent circuit properties

R_{s}	L_{s}	C_{s}	C_{p}
2.22Ω	4.47mH	1.02nF	2.54nF

Fig. 4 shows experimental waveforms for this converter when driving a 1 kΩ load, measured using a Rigol DS1054Z oscilloscope. $\mathrm{PLL_{out}}$ in Fig. 4 is the output from the FPGAs PLL and when locked, represents the polarity of the estimated resonant current $i_{L_{\mathrm{s}}}$ (estimated using signals V_A and V_B). $\mathrm{PLL_{out}}$ is then used to derive the gate signals, V_{gs1} and V_{gs2} for MOSFETs S_1 and S_2 respectively.

A similar converter is constructed within Simulink using the Simscape electrical package. A state machine-based controller is constructed to drive the two MOSFETs with parameters set to match the IRF510. After initialization (with fixed mode time durations calculated using the proposed model), the state machine determines the ideal mode durations based on the resonant current and the $v_{C_{\mathrm{p}}}$ voltage, as described in section II.

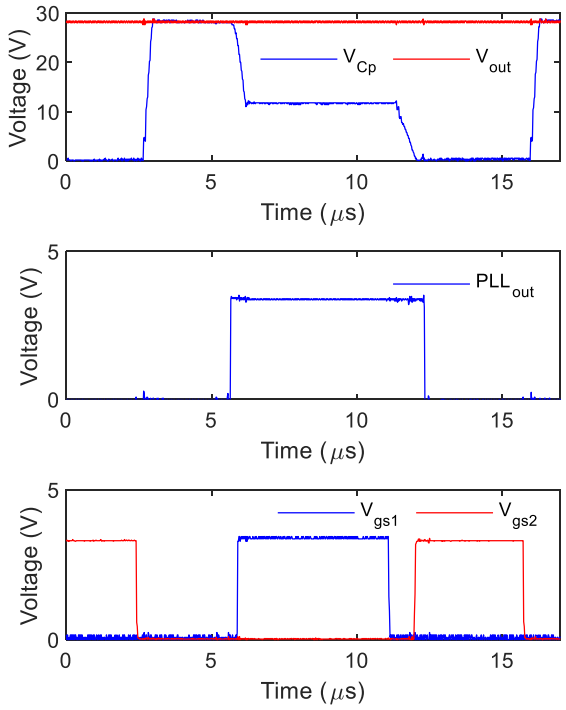

Fig. 4 – Experimental waveforms for the SUPR converter when driving a 1kΩ load with a 26% S_2 duty cycle [22]. The piezo resonator and output voltages (top), the PLL output signal (middle) and MOSFET gate signal (bottom) are shown

To provide validation, two voltage gain $M_{\text{out}} = V_{\text{out}}/V_{\text{DC}}$ measurement experiments are performed. First, the duty cycle of the low-side switch, S_2 $\left({}^{(\theta_4 - \pi)}/_{2\pi}\right)$ is varied through a range of 20-32%, and M_{out} is measured using an oscilloscope when driving a 1 kΩ load. Second, the converter is operated with the duty cycle fixed at 26% and the load varied between 500 and 10 kΩ. Similar analysis is performed using the Simulink model for comparison. Finally, the proposed describing function model is used to estimate M_{out} under the same load and duty cycle conditions. The results of these experiments are shown in Fig. 5 and Fig. 7.

Fig. 5 shows the voltage gain predicted by the proposed model ('Descrb. Func'), the model in [14] (using frequencies calculated using the proposed model), Simulink simulations and experimental results with changes in S_2 duty cycle $\left({}^{(\theta_4 - \pi)}/_{2\pi}\right)$, when driving a 1 kΩ load. The voltage gain estimated by the proposed model shows good agreement with both the experimental and Simulink measurements, with a slight overestimation at high S_2 duty cycles. Overall, the model shows close agreement with the experimental results, exhibiting a mean absolute percentage error (MAPE) of 1.44% and a standard deviation in the percentage error of 1.12%, where MAPE is defined as

$$\text{MAPE} = \frac{1}{n}\sum_{i=0}^{n}\left|\frac{V_{\text{out,Model}}(i) - V_{\text{out,Exp}}(i)}{V_{\text{out,Exp}}(i)}\right| \qquad (47)$$

This compares to a 4.2 – 39.5% MAPE and a standard deviation in the percentage error of 2.1 - 2.9% from the model in [14], depending on frequencies used, either those estimated by the proposed model or those from the experimental results.

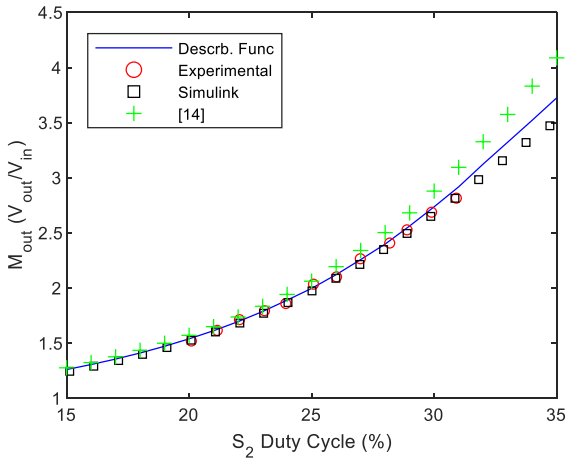

Fig. 5 – Voltage gain M_{out} vs S_2 duty cycle, with a load R_L=1kΩ

The overestimation that is observed is due mainly to inaccuracies in the modelling of the diode voltage drop, inaccuracies in the resonator properties (again mainly R_s) and unmodelled parasitic effects.

The mode durations and operating frequency estimated by the describing function model when generating the results presented in Fig. 5 are shown in Fig. 6 For convenience, the following mode duration angles are defined

$$\alpha = \theta_1 - 0 \qquad (48)$$

$$\beta = \theta_2 - \theta_1 \qquad (49)$$

$$\rho = \theta_5 - \theta_4 \qquad (50)$$

Fig. 7 shows the voltage gain predicted by the proposed model ('Descrb. Func'), Simulink simulations and experimental results with variations in load, when driven with a duty cycle $\left({}^{(\theta_4 - \pi)}/_{2\pi}\right) = 26\%$. The estimated voltage gain agrees well with the experimental results obtained from the practical converter, achieving greater accuracy estimations than the Simulink model, which overestimates the gain of the converter at larger value loads. However, at the maximum load tested, the experimental gain is lower than estimated by both the proposed model and Simulink. As a result, the model shows a MAPE of 2.03% compared to experimental measurements, with a standard deviation in the percentage error of 1.95%.

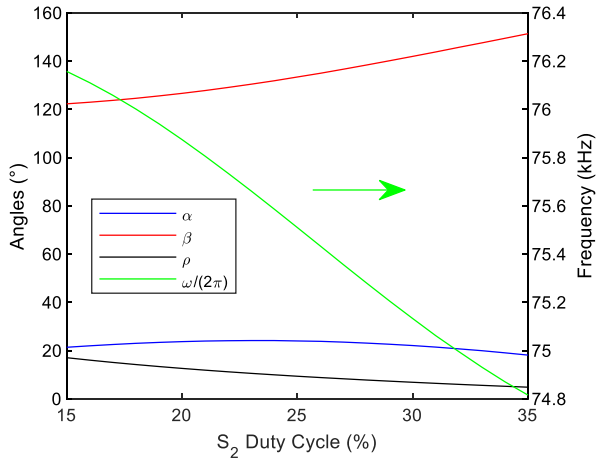

Fig. 6 – Mode angles vs S_2 duty cycle, with a 1kΩ load

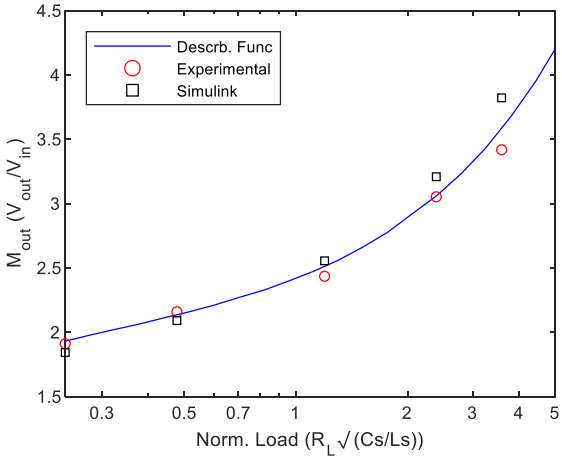

Fig. 7 - M_{out} vs normalised load (to the resonator characteristic impedance $\sqrt{L_s/C_s}$) with 26% S_2 duty cycle

V. Resonator Sensitivity Analysis

A. Accuracy of the proposed model against LTSpice

A sensitivity analysis is performed by varying the resonator equivalent circuit properties (R_s, L_s, C_s and C_p) and observing changes in gain. This analysis is performed using both the model derived here and LTSpice. This allows the error of the model with changes in resonator properties to be evaluated.

The converter simulated in LTSpice was operated with an $R_L = 2\text{k}\Omega$ ($\cong \sqrt{L_s/C_s}$) and a 12V DC supply. The converter was operated near its series resonant frequency, such that the negative going zero crossing of i_{L_s} occurs when S_2 turns on. S_2 was operated at a duty cycle $\left({(\theta_4 - \pi)}/{2\pi}\right) = 25\%$ for all variations. Given the complexity associated with determining an appropriate value for the S_1 duty cycle $\left({(\theta_2 - \theta_1)}/{2\pi}\right)$, the mode timting predicted by the proposed model was manually tuned in LTSpice until the response was deemed appropriate (i.e where the v_{C_p} waveform crosses zero closest to the resonant current zero crossing at θ_3).

For this analysis, the characteristic impedance $Z_0 = \sqrt{L_s/C_s}$, resonant frequency f_0, damping resistance R_s and parallel capacitance C_p of the SMD30T21F1000S resonator were each individually varied. The ranges of variation were selected by assuming radial-mode PRs typically have radii, a, of 7.5mm to 25mm and thickness, h, of 0.5mm to 5mm. Based on the ranges of a and h, the ranges of C_p, Z_0 and resonant frequency can be calculated using the model presented in [31] for the extreme values of a and h. Therefore, the range of variation is chosen to be 0.1 to 10 times the nominal value given in Table 1 for C_p and Z_0 and 0.6 to 2 times the nominal value for f_0. It is difficult to select a good range for R_s variation because its value depends on the physical construction of the device and its mounting. A range of 0.1 to 10 times the nominal value was chosen based on a study of existing resonators. It should be noted this investigation assumes that behaviour of the PR is dominated by radial mode vibration and other vibration modes (inc. spurious modes) was omitted from this analysis.

For each step in the parameter sweep, the gain of the converter $V_{\text{out,avg}}/V_{\text{DC}}$, where $V_{\text{out,avg}}$ is the cycle average, was estimated by the model and measured using LTSpice and the percentage error calculated to determine the accuracy of the model.

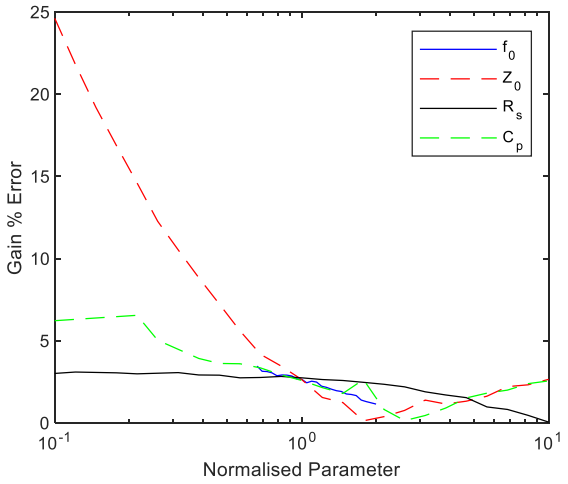

Fig. 8 – Sensitivity analysis evaluating the accuracy of the model when estimating gain with changes in resonator properties

Observing Fig. 8, the model shows acceptable accuracy across the range of variation, with only a ~3% error at the nominal point and a maximum error of 25%. It is noticeable that the error is largest when each of the parameters are at values below the nominal value, this is especially clear with C_p and Z_0. At parameter values greater than nominal, error in the gain predicted by the model was <3%. Errors are likely due to the assumptions and simplifications that are used within the model, this is especially true of Z_0, where we assume that the resonant current only contains a fundamental component, which is increasingly invalid at lower Z_0.

B. Effect of the Resonator on converter performance

The previously performed 'one-at-a-time' sensitivity analysis can subsequently be used to analyse the impact of changing resonator properties on the gain and additionally the

efficiency and the operating frequency of the converter. This gives insight into optimal resonator designs for this converter.

As can be seen in Fig. 9, increases in damping resistance R_S cause an approximately quadratic decrease in voltage gain. This is as expected as more power is lost in the resonator, less power is supplied to the load and thus lower output voltages (gains) are observed. Increases in C_p cause corresponding increases in voltage gain and thus cause increased resonant current to flow though the resonator. Changes in f_0 cause an almost identical effect to changes in C_p (as $\left|Z_{C_\mathrm{p}}\right| = 1/(\omega C_\mathrm{p})$), with increases in resonant frequency (or C_p), increasing the gain of the converter. Z_0 has a minimal impact on the voltage gain, with only a slight decrease in gain with increases in Z_0.

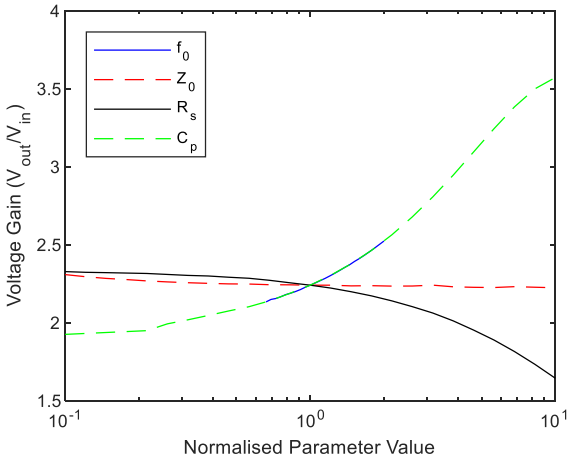

Fig. 9 – Voltage gain sensitivity analysis

The efficiency of the SUPR converter is given by

$$\eta = \frac{E_\mathrm{out}}{E_\mathrm{in}} = \frac{V_\mathrm{out}^2 2\pi}{V_\mathrm{DC} I_{L_\mathrm{s}} R_L [\cos(\theta_1) - \cos(\theta_2)]} \tag{51}$$

Fig. 10 shows the efficiency (calculated using (51)) with changes in each of the parameters. Z_0 has minimal impact on the efficiency of the converter, with only a slight increase with increase in Z_0. Increases in C_p, f_0 and R_s cause a similar decrease in efficiency, with an approximately quadratic trend. Again, changes in f_0 and C_p cause an almost identical change in efficiency whereas changes in R_s cause a slightly shallower drop in efficiency, compared to C_p.

As can be seen in Fig. 11, the greatest change in normalised operating frequency occurs with changes in Z_0; this is common property of resonant converters. As Z_0 decreases from the nominal value, a sharp increase in normalised frequency is required for optimal operation. Similarly, increases in Z_0 cause a decrease in operating frequency. Z_0 has a larger effect on operating frequency than the other 3 parameters in this study. Both f_0 and C_p have a similar effect, agreeing with the results shown in Fig. 8 and Fig. 9, with decreases in value causing slight increases in operating frequency, and with increases in value causing a drop in operating frequency. Finally, R_s has negligible impact on operating frequency, as one would expect

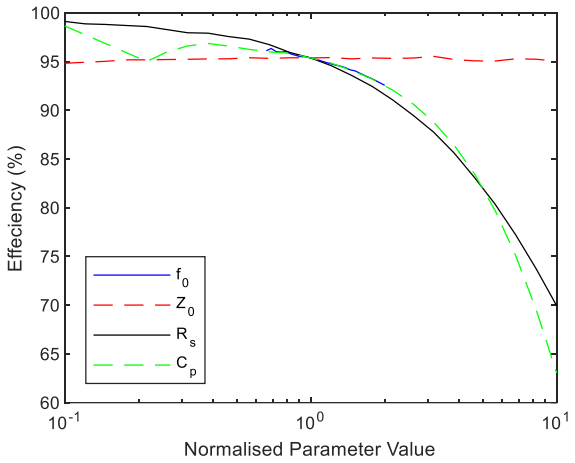

Fig. 10 – Efficiency sensitivity analysis

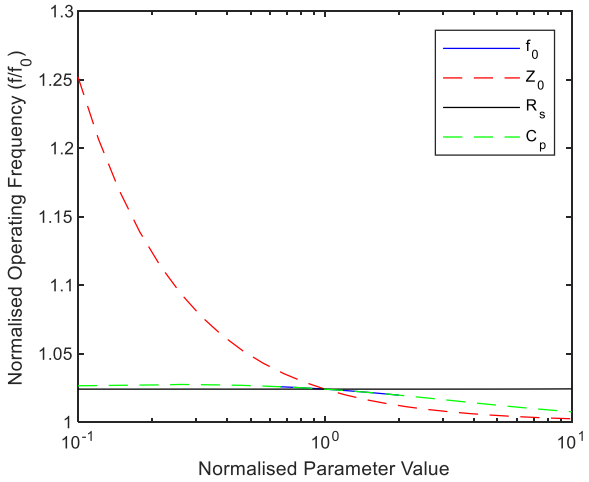

Fig. 11 – Operating frequency sensitivity analysis

VI. Design Considerations

Based on Fig. 9 and Fig. 10, care should be taken to choose an appropriate resonator for this converter. Ideally, the resonator should have no losses ($R_\mathrm{s} = 0$), large C_p and high resonant frequency, to maximise the output voltage gain that can be achieved. Whilst minimising R_s has no negative effects on the performance of the converter, choosing a large C_p and high resonant frequency can cause adverse effects. As Fig. 10 shows, increasing C_p or f_0 causes the efficiency of the converter to decrease, as shown in (21) from [14]. For a practical resonator, a larger radius could be used to increase C_p for higher efficiency, however, as a result of the larger radius, the resonant frequency decreases (reducing the efficiency of the converter), resulting in an overall minimal change in efficiency. Therefore, C_p and f_0 should be designed to be a balance between achieving higher output voltages and reducing efficiency.

In contrast, Z_0 causes minimal impact of the performance of the converter, other than to change the operating frequency of the converter. Whilst this is not necessarily a negative, an increase in normalised operating frequency increases the chances of interacting with spurious modes, which could cause

a decrease in efficiency and reliability, and therefore should be avoided [13]. Additionally, low Z_0 invalidates some of the analysis presented here and in common analysis techniques, therefore the design process becomes more complex as the effect of additional harmonics need to be accounted for.

Determining R_s of a resonator design is complex as it is a combination of several loss mechanisms occurring in piezoelectrics. However, some steps can be taken at the design stage to minimise R_s, such as using a high Q ('hard') piezoelectric material, achieving a high-quality construction with minimal defects, and carefully designing mounting mechanisms as to not damp the vibrational characteristics of the resonator.

The other elements of the converter should also be carefully chosen as not to impair performance. First, the output capacitance should be chosen to minimise ripple on the output voltage, with larger capacitances causing lower ripple but with the trade-off of larger size and longer initial charging times. The MOSFETs should be chosen to have very low (<1Ω) on state resistance (lowering losses) and with low C_{DS} capacitance, as this capacitance is in parallel with C_p, increasing the effective parallel capacitance of the resonator. Finally, diodes should ideally be Schottky diodes with low forward voltage drops and sufficiency high PIV rating. Ideally, diodes would be replaced with additional MOSFETs as in [14] but this increases control and drive complexity.

VII. Conclusion

A model of the SUPR converter is presented, based on the describing function method. A full derivation of the model is shown, and a method for the solution of the operational mode durations is proposed. The model is validated against experimental and simulated results, with good accuracy. Further analysis is performed using this model to determine how the operational conditions (load and desired output voltage) affect the performance of the converter. Finally, a sensitivity analysis of the resonator parameters is presented, allowing an informed discussion on the design of the resonator for optimal performance.

VIII. References

[1] E. Wells, 'Comparing magnetic and piezoelectric transformer approaches in CCFL applications', p. 7, 2002.

[2] A. M. Flynn and S. R. Sanders, 'Fundamental limits on energy transfer and circuit considerations for piezoelectric transformers', *IEEE Transactions on Power Electronics*, vol. 17, no. 1, pp. 8–14, Jan. 2002, doi: 10.1109/63.988662.

[3] A. V. Carazo, '50 years of piezoelectric transformers. Trends in the technology', *MRS Online Proceedings Library Archive*, vol. 785, 2003.

[4] J. Forrester *et al.*, 'Comparison of BSPT and PZT Piezoelectric Ceramic Transformers for High-Temperature Power Supplies', *Adv Eng Mater*, p. 2200513, Sep. 2022, doi: 10.1002/adem.202200513.

[5] A. Vazquez Carazo, 'Piezoelectric Transformers: An Historical Review', *Actuators*, vol. 5, no. 2, p. 12, Apr. 2016, doi: 10.3390/act5020012.

[6] Y.-P. Liu, D. Vasic, F. Costa, and D. Schwander, 'Piezoelectric 10W DC/DC converter for space applications', in *Proceedings of the 2011 14th European Conference on Power Electronics and Applications*, Aug. 2011, pp. 1–7.

[7] J. Navas, T. Bove, J. A. Cobos, F. Nuno, and K. Brebol, 'Miniaturised battery charger using piezoelectric transformers', in *APEC 2001. Sixteenth Annual IEEE Applied Power Electronics Conference and Exposition (Cat. No.01CH37181)*, Mar. 2001, pp. 492–496 vol.1. doi: 10.1109/APEC.2001.911692.

[8] Y. C. Wang *et al.*, 'Theory and experiment of high voltage step-up ratio disk type piezoelectric transformer for LCD-TV', in *IEEE International Conference on Mechatronics, 2005. ICM '05.*, Jul. 2005, pp. 284–287. doi: 10.1109/ICMECH.2005.1529270.

[9] W. Feng, F. C. Lee, and P. Mattavelli, 'Optimal Trajectory Control of Burst Mode for LLC Resonant Converter', *IEEE Transactions on Power Electronics*, vol. 28, no. 1, pp. 457–466, Jan. 2013, doi: 10.1109/TPEL.2012.2200110.

[10] M. Khanna, R. Burgos, Q. Wang, K. D. T. Ngo, and A. V. Carazo, 'New Tunable Piezoelectric Transformers and Their Application in DC-DC Converters', *IEEE Transactions on Power Electronics*, vol. 32, no. 12, pp. 8974–8978, Dec. 2017, doi: 10.1109/TPEL.2017.2702124.

[11] Z. Yang, J. N. Davidson, and M. P. Foster, 'Output voltage regulation for piezoelectric transformer-based resonant power supplies using phase-locked loop', in *The 10th International Conference on Power Electronics, Machines and Drives (PEMD 2020)*, Dec. 2020, pp. 455–460. doi: 10.1049/icp.2021.1099.

[12] D. Vasic, Y.-P. Liu, F. Costa, and D. Schwander, 'Piezoelectric transformer-based DC/DC converter with improved burst-mode control', in *2013 IEEE Energy Conversion Congress and Exposition*, Sep. 2013, pp. 140–146. doi: 10.1109/ECCE.2013.6646693.

[13] J. Forrester, J. N. Davidson, M. P. Foster, and D. A. Stone, 'Influence of Spurious Modes on the Efficiency of Piezoelectric Transformers: a Sensitivity Analysis', *IEEE Transactions on Power Electronics*, pp. 617–629, 2020, doi: 10.1109/TPEL.2020.3001486.

[14] B. Pollet, G. Despesse, and F. Costa, 'A New Non-Isolated Low-Power Inductorless Piezoelectric DC–DC Converter', *IEEE Trans. Power Electron.*, vol. 34, no. 11, pp. 11002–11013, Nov. 2019, doi: 10.1109/TPEL.2019.2900526.

[15] J. D. Boles, J. J. Piel, and D. J. Perreault, 'Enumeration and Analysis of DC–DC Converter Implementations Based on Piezoelectric Resonators', *IEEE Transactions on Power Electronics*, vol. 36, no. 1, pp. 129–145, Jan. 2021, doi: 10.1109/TPEL.2020.3004147.

[16] M. Touhami, G. Despesse, and F. Costa, 'A New Topology of DC-DC Converter Based On Piezoelectric Resonator', in *2020 IEEE 21st Workshop on Control and Modeling for Power Electronics (COMPEL)*, Nov. 2020, pp. 1–7. doi: 10.1109/COMPEL49091.2020.9265767.

[17] J. Du, J. Hu, and K.-J. Tseng, 'High-power, multioutput piezoelectric transformers operating at the thickness-shear

vibration mode', *IEEE Transactions on Ultrasonics, Ferroelectrics, and Frequency Control*, vol. 51, no. 5, pp. 502–509, May 2004, doi: 10.1109/TUFFC.2004.1320823.

[18] M. Touhami *et al.*, 'Piezoelectric Materials for the DC-DC Converters Based on Piezoelectric Resonators', in *2021 IEEE 22nd Workshop on Control and Modelling of Power Electronics (COMPEL)*, Nov. 2021, pp. 1–8. doi: 10.1109/COMPEL52922.2021.9645999.

[19] J. D. Boles, J. E. Bonavia, P. L. Acosta, Y. K. Ramadass, J. H. Lang, and D. J. Perreault, 'Evaluating Piezoelectric Materials and Vibration Modes for Power Conversion', *IEEE Transactions on Power Electronics*, vol. 37, no. 3, pp. 3374–3390, Mar. 2022, doi: 10.1109/TPEL.2021.3114350.

[20] J. J. Piel, J. D. Boles, J. H. Lang, and D. J. Perreault, 'Feedback Control for a Piezoelectric-Resonator-Based DC-DC Power Converter', in *2021 IEEE 22nd Workshop on Control and Modelling of Power Electronics (COMPEL)*, Nov. 2021, pp. 1–8. doi: 10.1109/COMPEL52922.2021.9646012.

[21] M. Touhami, G. Despesse, F. Costa, and B. Pollet, 'Implementation of Control Strategy for Step-down DC-DC Converter Based on Piezoelectric Resonator', in *2020 22nd European Conference on Power Electronics and Applications (EPE'20 ECCE Europe)*, Sep. 2020, pp. 1–9. doi: 10.23919/EPE20ECCEEurope43536.2020.9215910.

[22] J. Forrester, J. N. Davidson, and M. P. Foster, 'Resonant current estimation and phase-locked loop control system for inductorless step-up single piezo element-based (SUPRC) DC-DC converter', presented at the IECON 2022, Brussels, Belgium, Brussels, Belgium, Oct. 2022.

[23] B. Pollet, F. Costa, and G. Despesse, 'A new inductorless DC-DC piezoelectric flyback converter', in *2018 IEEE International Conference on Industrial Technology (ICIT)*, Feb. 2018, pp. 585–590. doi: 10.1109/ICIT.2018.8352243.

[24] K. S. Meyer, M. A. E. Andersen, and F. Jensen, 'Parameterized analysis of Zero Voltage Switching in resonant converters for optimal electrode layout of Piezoelectric Transformers', in *2008 IEEE Power Electronics Specialists Conference*, Jun. 2008, pp. 2543–2548. doi: 10.1109/PESC.2008.4592323.

[25] E. L. Horsley, A. V. Carazo, N. Nguyen-Quang, M. P. Foster, and D. A. Stone, 'Analysis of Inductorless Zero-Voltage-Switching Piezoelectric Transformer-Based Converters', *IEEE Transactions on Power Electronics*, vol. 27, no. 5, pp. 2471–2483, May 2012, doi: 10.1109/TPEL.2011.2169431.

[26] M. S. Rodgaard, T. Andersen, and M. A. E. Andersen, 'Empiric analysis of zero voltage switching in piezoelectric transformer based resonant converters', in *6th IET International Conference on Power Electronics, Machines and Drives (PEMD 2012)*, Bristol, UK: IET, 2012, pp. A63–A63. doi: 10.1049/cp.2012.0217.

[27] M. P. Foster, J. N. Davidson, E. L. Horsley, and D. A. Stone, 'Critical Design Criterion for Achieving Zero Voltage Switching in Inductorless Half-Bridge-Driven Piezoelectric-Transformer-Based Power Supplies', *IEEE Transactions on Power Electronics*, vol. 31, no. 7, pp. 5057–5066, Jul. 2016, doi: 10.1109/TPEL.2015.2481706.

[28] 'SymPy'. https://www.sympy.org/en/index.html (accessed Nov. 08, 2022).

[29] K. Schittkowski, 'NLPQL: A fortran subroutine solving constrained nonlinear programming problems', *Ann Oper Res*, vol. 5, no. 2, pp. 485–500, Jun. 1986, doi: 10.1007/BF02022087.

[30] J. Forrester *et al.*, 'Equivalent circuit parameter extraction of low-capacitance high-damping PTs', *Electronics Letters*, Jan. 2020, doi: 10.1049/el.2019.3887.

[31] O. Stefan, 'Electric equivalent circuit of the circular piezoelectric resonator', *Czech J Phys*, vol. 20, no. 4, pp. 432–440, Apr. 1970, doi: 10.1007/BF01698401.

IX. APPENDIX

The following is Python code for the generation of the $v_{C_{p}<1>}$ equation given in (33) using the Sympy library:

```
from sympy import pi, cos, sin, symbols, integrate,
simplify, I

omega, Cp, Ils, theta, Vdf, Vout, Vdc, Rds = symbols('omega
Cp Ils theta Vdf Vout Vdc Rds')
theta1, theta2, theta3, theta4, theta5, theta6 =
symbols('theta1 theta2 theta3 theta4 theta5 theta6')

#define vcp
M1 =  1 / omega / Cp * Ils *cos(theta) + (Vdf * omega * Cp
+ Cp * Vout * omega - Ils) / omega / Cp
M2 =  Vdc - Vdf - Ils * sin(theta) * Rds
M3 =  1 / omega / Cp * Ils * cos(theta) - (Ils *
sin(theta2) * Rds * omega * Cp - Vdc * omega * Cp + Vdf *
omega * Cp + Ils * cos(theta2)) / omega / Cp
M4 =  -Ils * sin(theta) * Rds
M5 =  1 / omega / Cp * Ils * cos(theta) - Ils * (Cp *
sin(theta4) * Rds * omega + cos(theta4)) / omega / Cp
M6 =  Vout+Vdf

#Define imaginary elements
vcp_1c = 1/pi*integrate(cos(theta)*M1, (theta, 0, theta1))
vcp_2c = 1/pi*integrate(cos(theta)*M2, (theta, theta1,
theta2))
vcp_3c = 1/pi*integrate(cos(theta)*M3, (theta, theta2, pi))
vcp_4c = 1/pi*integrate(cos(theta)*M4, (theta, pi, theta4))
vcp_5c = 1/pi*integrate(cos(theta)*M5, (theta, theta4,
theta5))
vcp_6c = 1/pi*integrate(cos(theta)*M6, (theta, theta5,
2*pi))
vcp_c = simplify(vcp_1c+vcp_2c+vcp_3c+vcp_4c+vcp_5c+vcp_6c)

#Define real elements
vcp_1s = 1/pi*integrate(sin(theta)*M1, (theta, 0, theta1))
vcp_2s = 1/pi*integrate(sin(theta)*M2, (theta, theta1,
theta2))
vcp_3s = 1/pi*integrate(sin(theta)*M3, (theta, theta2, pi))
vcp_4s = 1/pi*integrate(sin(theta)*M4, (theta, pi, theta4))
vcp_5s = 1/pi*integrate(sin(theta)*M5, (theta, theta4,
theta5))
vcp_6s = 1/pi*integrate(sin(theta)*M6, (theta, theta5,
2*pi))
vcp_s = simplify(vcp_1s+vcp_2s+vcp_3s+vcp_4s+vcp_5s+vcp_6s)

#Define vcp<1>
vcp_a=vcp_s+I*vcp_c
print(vcp_a)
```

Jack Forrester received the M.Eng degree in electrical and electronic engineering in 2017 and the Ph.D degree in piezoelectric transformer analysis and design in 2022 both from the University of Sheffield, Sheffield, U.K. He is currently a academic fellow at the University of Sheffield, researching power supply technologies for plasma generation. His current research interests are in the area of piezoelectric based power converters, with a focus on transformer design and characterisation.

Jonathan N. Davidson received the M.Eng. degree in electronic engineering and the Ph.D. degree in thermal modelling and management from the University of Sheffield, Sheffield, U.K., in 2010 and 2015, respectively.

In 2015, he became a Lecturer in electrical engineering at the University of Sheffield. He was made Senior Lecturer in 2022. His research interests include thermal modelling and management of power electronics, and the design and analysis of piezoelectric transformer-based and resonant power converters, high-voltage power supplies for plasma chemistry and waste-water sensing systems.

Martin P. Foster received the B.Eng. degree in electronic and electrical engineering, the M.Sc.(Eng.) degree in control systems, and the Ph.D. degree for his thesis “Analysis and Design of High-order Resonant Power Converters” all the University of Sheffield, Sheffield, U.K., in 1998, 2000, and 2003, respectively.

Since 2003, he has been a member of the academic staff in the Department of Electronic and Electrical Engineering, The University of Sheffield, where he is involved in power electronic systems. His current research interests include the modelling and control of switching power converters, resonant power supplies, multilevel converters, battery management, piezoelectric transformers, power electronic packaging, and autonomous aerospace vehicles.